Hindawi
Journal of Chemistry
Volume 2024, Article ID 2779104, 11 pages
https://doi.org/10.1155/2024/2779104

Research Article

Sea Urchin-Like MnO_2/Biomass Carbon Composite Electrode Material for High-Performance Supercapacitors

Xiaoyu Zhao,[1] Ning Wang,[2] Lei Li,[2] Zixun Fang,[2] Shoufeng Tang,[2] and Jianmin Gu[2]

[1]*Department of Food and Pharmaceutical Engineering, Suihua University, Suihua 152000, China*
[2]*State Key Laboratory of Metastable Materials Science and Technology (MMST), Hebei Key Laboratory of Applied Chemistry, Yanshan University, Qinhuangdao 066004, China*

Correspondence should be addressed to Shoufeng Tang; tangshf@ysu.edu.cn and Jianmin Gu; jmgu@ysu.edu.cn

Received 20 December 2022; Revised 23 January 2024; Accepted 2 February 2024; Published 27 February 2024

Academic Editor: Takeshi Kondo

Manganese oxide materials for high-performance supercapacitors are as popular electrode materials of energy storage devices based on their high theoretical capacitance. However, its development is limited by its poor electrical conductivity and insufficient contact surface area, which causes the supercapacitor to fail to achieve its theoretical specific capacitance. In this paper, unique sea urchin-like MnO_2/biomass carbon (BC) composite materials were prepared for supercapacitors, showing the lower resistance compared with pure MnO_2, which possesses superior electrochemical performance due to the advances in outstanding electrical conductivity. The single electrode test results show that the composite material achieves a specific capacitance of 205.5 $F{\cdot}g^{-1}$ at the current density of 0.5 $A{\cdot}g^{-1}$; with the current density increasing by a factor of 20, the supercapacitor loaded with this composite still retained 63.2% of its initial capacitance, showing its high rate performance. Meanwhile, the constructed asymmetric supercapacitor can change the color of electrochromic devices and drive the light of electrochemiluminescent devices, indicating its promising application. This work provided a promising route for the rational construction of multiple dimensioned high-performance electrode materials for use in new energy storage devices.

1. Introduction

With the rapid depletion of fossil fuels, the reliable and efficient conversion/storage of green energy has attracted considerable attention worldwide [1–6]. Compared with other energy storage devices [7–15], supercapacitors (SCs) have been widely used in the fields of portable electronics, heavy industry, national defense, electric vehicles, and electronic applications based on their advantages, such as high power density, rapid charge-discharge capability, and stability [16–21]. In recent years, MnO_2 has become the most potential material in the field of SCs due to its advantages such as low cost, high theoretical capacitance, and large voltage window in water system electrolytes [22–26]. However, it is limited by the poor conductivity of manganese oxide electrode material and the instability in the cycle process, which reduces its ionic and electron transport speed and its electrochemical properties. Therefore, the development of new electrode materials for high-performance SCs still has challenges [27–32].

In order to solve the problem of MnO_2 used as an SC electrode, the electrochemical performance of composite carbon materials has been proven to work effectively [33, 34]. Therefore, MnO_2 used for electrode materials must be combined with conductive carbon black [35], carbon nanotubes [36], graphene [37], activated carbon [38], or biocarbon [39] to improve the electrochemical energy. Biomass carbon (BC) based on pomelo peel is now a promising carbon material, which has good applications in the field of electrochemistry, catalysis, and other aspects [40–46]. Using the special structure of biomass, the porous carbon material with a high-specific surface area, long cycle stability, large porosity, and good electrical conductivity can be obtained by simple carbonization and subsequent treatment. The porous carbon material combined with manganese oxide is expected to improve the electrochemical

performance of manganese oxide [44–50]. The introduction of biomass carbon with strong electrical conductivity can greatly increase the electrical conductivity of the whole system.

Herein, we used a simple hydrothermal method to compound the highly conductive biomass carbon prepared from pomelo skin with MnO_2 nanorods to form a unique sea urchin-like MnO_2/BC nanocomposite, in which the biomass carbon material with a larger specific surface area and porous structure further enables the electrochemical performance of the obtained electrode materials to meet the expectations. The specific capacitance of MnO_2/BC composites' electrode can reach 205.5 $F \cdot g^{-1}$ when the charge-discharge current density is 0.5 $A \cdot g^{-1}$. In addition, the asymmetric supercapacitor constructed by using MnO_2/BC composite as the positive electrode and BC as the negative electrode maintains 105% of the initial capacitance after 4000 long cycles, showing good long-cycle stability. Therefore, the MnO_2/BC composite electrode as an excellent candidate provided a promising route for high-performance SCs.

2. Experiment

2.1. Chemicals. Potassium hydroxide (KOH, 96.0%) and potassium permanganate ($KMnO_4$, 99.5%) were purchased from Tianjin Kermel Chemical Reagent Co. Ltd. Hydrochloric acid (HCl, 37%), and ethyl alcohol (CH_3CH_2OH, 99.7%) was purchased from Qinhuangdao Chemical Co. Ltd. All the reagents were employed directly without further refinement. The water used throughout all experiments was purified through a Millipore system.

2.2. Preparation of Biomass Carbon. Remove the inner flesh of grapefruit peel and keep the outer skin and put it in an oven at 90°C until drying. Then, the pomelo peel is cut into smaller pieces, which are crushed in a shredder to get pomelo peel powder. A certain amount of dried pomelo peel powder was taken in a porcelain boat, and then the first precarbonization was carried out in a tubular furnace for 2 h at 700°C with a heating rate of 2°C·min^{-1}. High-purity N_2 was passed through the tube furnace at a flow rate of 50 ml·min^{-1}. The precarbonized powder was washed repeatedly with dilute hydrochloric acid and water to remove impurity ions until pH = 7. The above centrifuged product was dried at 60°C for 10 hours. According to the mass ratio of 1 : 2, we mix a certain mass of the above samples and potassium hydroxide, and after mixing, we grind with a mortar and then mechanical ball mill for 3 hours. After ball-milling, 2 g of the mixture was placed in a porcelain boat and recarbonized at 800°C for 2 h in a tube furnace. The carbonized black powder was washed repeatedly with dilute hydrochloric acid and water to remove impurity ions until pH = 7. The above centrifuged products were dried at 60°C for 10 hours to obtain biomass carbon (BC).

2.3. Preparation of MnO_2/BC Composite. Firstly, 150 mg BC was placed in 15 mL deionized water, and then a certain amount of dilute hydrochloric acid was added to BC for about 30 minutes. Then, we add 0.298 g of potassium permanganate to the above solution and stir it with a glass rod for 10 minutes until it fully dissolved. Finally, the mixture was transferred to a 20 mL reaction kettle resistant to high pressure and kept at 150°C for 12 hours. After the reaction was completed, the reaction products were removed, centrifuged, and washed with ultrapure water and ethanol at 6000 R/min, and the collected samples were placed in a drying oven and dried at 80°C for 10 hours with the mass ratio of MnO_2 and BC≈1.1 : 1. In addition, we add pure manganese dioxide only without adding biomass carbon, and other steps are the same. The weight of the electrodes was all about 2 mg.

2.4. Characterization. The synthesized samples were characterized by XRD (Bruker AXS D8 diffractometer with Cu Kα radiation), SEM (JEOL JSM-840), the CHI660E electrochemical workstation, and the LAND CT2001. The battery tester was employed to measure the system with Ag/AgCl electrode and platinum sheet as the reference and counter electrode in the electrolyte of 6 M KOH aqueous solution, respectively.

2.5. Construction of Supercapacitors. The half-cell test of MnO_2/BC composite material and BC electrode material in the test was completed in the system with Ag/AgCl electrode as the reference electrode, platinum sheet as the counter electrode, and active material as the working electrode. Active material, acetylene black, and teflon were mixed in an 8 : 1 : 1 ratio. Then, it spread on nickel foam as the working electrode and was pressed for 30 seconds under the pressure condition of 10 MPa and transferred to the oven after drying. In the two-electrode test, MnO_2/BC composite material was used as the positive electrode and BC synthesized from pomelo skin was used as the negative electrode. The positive and negative electrode materials follow the charge balance principle $q^+ = q^-$. The electrolyte used in the two-electrode test and three-electrode test was 1 M Na_2SO_4.

3. Results and Discussion

To synthesize composite electrodes, we first dried grapefruit peels and converted them into biomass carbon by carbonization. The biomass carbon obtained from grapefruit peel was activated by adding dilute hydrochloric acid and then mixed with potassium permanganate and heated hydrothermally at 150°C for 12 hours to obtain the manganese dioxide/biomass carbon (MnO_2/BC) composite. In addition, pure MnO_2 electrodes just do not have biomass carbon added, and all other steps are the same (Figure 1(a)). The morphologies of MnO_2 and MnO_2/BC composites were significantly different based on their TEM, which shows a great difference in the microstructure of the two electrode materials (Figures 1(b) and 1(c)). The pure MnO_2 has a 2-dimensional wire-like structure with an average length of about 1-2 microns (Figure 1(b)). However, after compositing with biomass carbon, MnO_2/BC showed a sea urchin-like structure, which is consistent with the results of

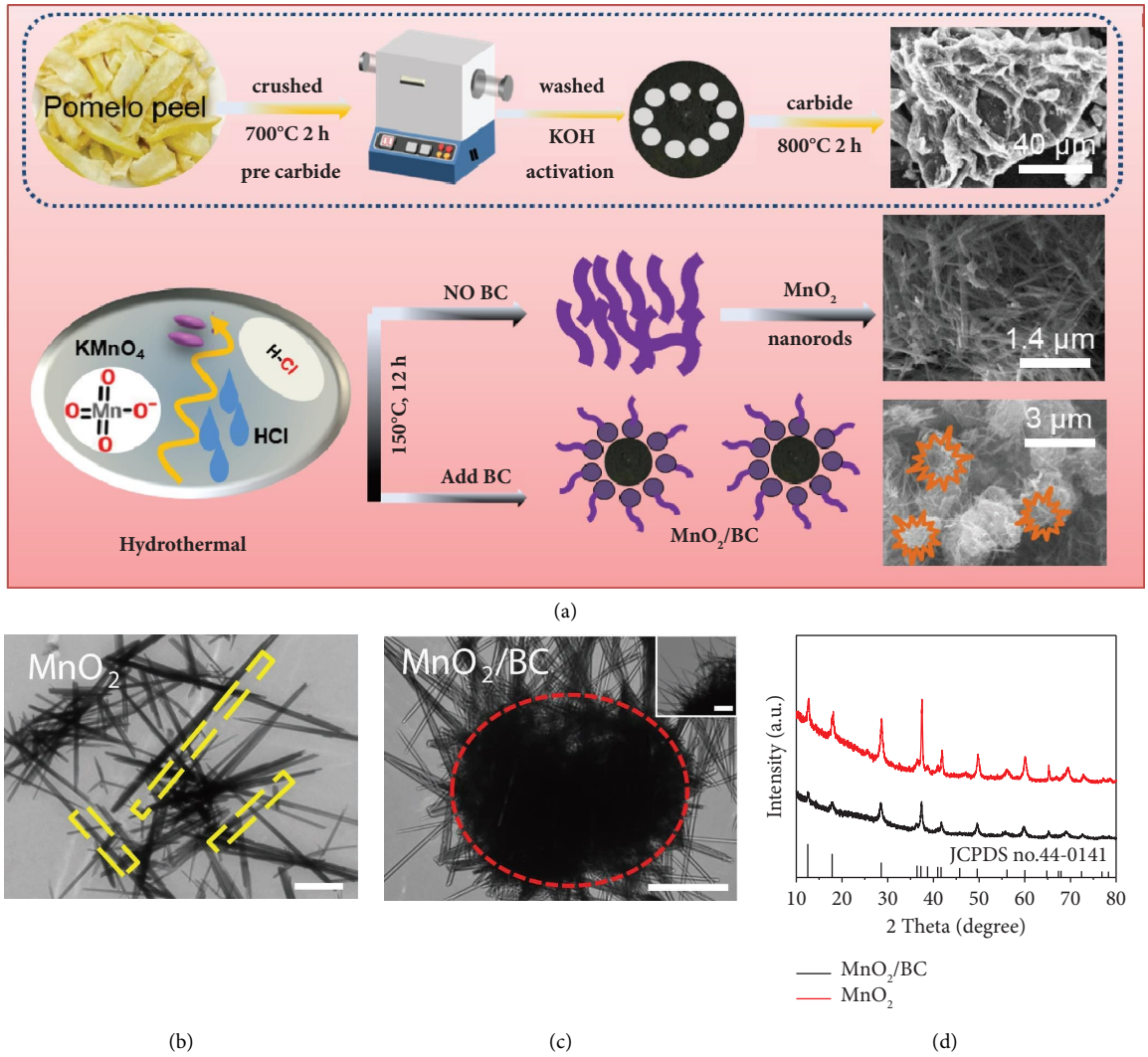

Figure 1: Schematic diagram of the process of preparing MnO_2 and MnO_2/BC electrode materials (a); the transmission images of the synthesized MnO_2 (b) and MnO_2/BC (c) are magnified transmission images with scales of (b-c) 500 nm and insets of 200 nm; XRD patterns of MnO_2 and MnO_2/BC (d).

transmission observation. The EDS test shows that manganese and oxygen elements are uniformly distributed in the prepared MnO_2/BC composite, indicating that the MnO_2 nanorods are densely distributed on the surface of BC, which may be attributed to the fact that the loose and porous carbon materials provide abundant sites for manganese oxides (Figures S1 and 1(d)).

In order to characterize the accurate structure of the MnO_2/BC composite electrodes and the pure MnO_2 electrodes, we provide the XRD of the electrode material before and after adding the biomass carbon (Figure 1(b)). Firstly, the XRD of MnO_2 corresponds to the diffraction peak of the standard card of MnO_2 (JCPDS No. 44-0141), which represents its high purity. The XRD of the MnO_2/BC composites shows diffraction peaks at 12.8°, 28.8°, 37.5°, 41.9°, 49.8°, and 60.3° correspond to (110), (310), (211), (301), (411), and (521) crystal planes, respectively, indicating that MnO_2/BC composites have been successfully prepared [45]. Both electrode materials show sharp peak shapes without excess miscellaneous peaks, indicating the high purity and crystallinity of the MnO_2/BC electrode materials synthesized in our study. In addition, compared with pure MnO_2, there is no obvious peak of biomass carbon in the diffraction peak of the composite material because the synthesized biomass carbon is amorphous.

To explore the element composition of the composite electrode material, the EDS test of MnO_2/BC was conducted, which shows that manganese, oxygen, and carbon elements are uniformly distributed in the prepared MnO_2/BC composite (Figure S1a). Besides, the EDS test of MnO_2 shows that manganese and oxygen elements are uniformly distributed in the prepared MnO_2 composite (Figure S1b). Typical N_2 adsorption-desorption isotherms were supplied to further evaluate the specific surface area of the prepared MnO_2/BC and pure MnO_2 electrode materials [24, 29]. The data for the specific surface area P/P_0 in the range of 0.45–0.9 show that (Figures S2a and S2b) the MnO_2/BC and pure MnO_2 electrode materials have a specific surface area of

139.291 $m^2 \cdot g^{-1}$ and 77.301 $m^2 \cdot g^{-1}$, respectively, which are the typical characteristics of mesoporous materials (Table S1). The results show that in the presence of biomass carbon, the composite has a larger specific surface area than the pure MnO_2 composite. The larger specific surface area of the composite can provide more active sites for electrochemical reactions. In the process of electrochemical testing, more pore structures can provide a good ion transfer pathway to supply electrolyte ions, which makes sufficient preparation for the improvement of the electrochemical performance of SC [42–55].

The CV curves of MnO_2/BC composite and pure MnO_2 at a scanning rate of 20 $mV \cdot s^{-1}$ in the potential range 0-1 V are shown in Figure 2(a), in which both electrode materials are approximately rectangular indicating that both materials rely on the double-layer effect to store charge. In addition, the MnO_2/BC electrode material exhibits a larger capacitance compared with pure MnO_2 at the same scanning rate. In order to better understand the electrochemical properties exhibited by MnO_2/BC, CV at different canning rates, tests were carried out under a voltage window of 0-1 V. that there is no obvious deformation of the curve as the sweep speed increases to 100 $mV \cdot s^{-1}$, indicating that the MnO_2/BC electrode material has good electrochemical reversibility and stability (Figure 2(b)). The contribution of capacitance and diffusion in the MnO_2/biomass carbon composite electrode is further analyzed in Figure S3. The peak current values are calculated by deriving the peak current values at different voltage scan rates after the following equation:

$$\text{Logi} = \text{blogv} + \text{Log}. \quad (1)$$

The *b*-value obtained after fitting the peak data is 0.8284 (Figure S3). Therefore, the MnO_2/biomass carbon composite electrode material exhibits battery properties and pseudocapacitive properties [56, 57].

In order to further understand the electrochemical properties of the MnO_2/BC electrode material, we examined the specific capacitance obtained at 0.5–10 $A \cdot g^{-1}$ (Figure 2(c)). The symmetrical charge-discharge curves indicate typical double-layer behavior. Besides, the curve still does not appear obvious voltage drop, which indicates that the resistance of the material is very small even at large current. With the current density at 0.5, 1, 2, 3, 5, 8, and 10 $A \cdot g^{-1}$, the specific capacitance of the composite material can be 205.5, 193, 176, 166, 150, and 144, respectively, while the electrochemical performance of pure manganese dioxide at the same current density is 115, 100, 90, 84, 75, 64, and 60 $F \cdot g^{-1}$ (Figure 2(d)). The MnO_2/BC electrode material with biomass carbon composite exhibits better rate performance (63.2%), which retains more initial capacitance than pure manganese dioxide (52.2%).

In order to characterize the electrical conductivity of the composite material after the composite of biomass carbon, we conducted the EIS of MnO_2/BC electrode material in the frequency ranging from 10^{-2} Hz to 10^5 Hz (Figure 2(e)). Both the composite material and the corresponding pure MnO_2 impedance map contain two parts: a semicircle in the high-frequency region and a straight line in the low-frequency region. Local amplification of illustrations is further shown in Figure 2(e). The composite materials in the high-frequency region of the semicircle have a smaller and more steep low-frequency region of the straight line, which shows that the MnO_2/BC electrode has smaller load transfer resistance, faster charge transport capacitance, and better ion diffusion ability due to a shorter ion diffusion pathway. In addition, the equivalent circuit diagram could be obtained by careful simulation of the resistance curves (the inset of Figure 2(e)), where Rs and Rct are used to represent the internal resistance and charge transfer resistance of SC, W signifies Warburg impedance, representing ion diffusion in the low-frequency region, and CPE is a constant phase angle element to simulate the capacitance properties of the electrode. Notably, the MnO_2/BC electrode exhibits a higher slope line, signifying the lower diffusion resistance, indicating a faster reaction kinetic rate compared with a pure MnO_2 electrode. After fitting data, the Rs and Rct values of the MnO_2/BC composite electrode material were 2.23 Ω and 6.29 Ω, both smaller than those of the pure MnO_2 electrode material (Table S2), which were consistent with the electrochemical experimental data. Therefore, sea urchin-like MnO_2/BC composite has enhanced electrical conductivity compared with pure MnO_2. To evaluate the suitability of supercapacitor materials for further practical applications, we conducted the long cycle performance test. As shown in Figure 2(f), the specific capacitance of MnO_2/BC composite can still maintain 96.1% of the initial specific capacitance, which is very competitive compared with 90.4% of the pure MnO_2 material at 0.5 $A \cdot g^{-1}$. The high cyclic stability indicates that MnO_2 enhances the stability of the material after composite porous BC, making the electrode material more stable during continuous charging and discharging.

We used the synthesized porous biomass carbon as an anode material for supercapacitors and further characterized its morphology and electrochemical properties. The SEM diagram of biomass carbon BC shows a loose 3D network structure and large loose porous bulk structures with ordered channels, where carbon elements were evenly distributed (Figures 3(a) and 3(b)). The phase composition biomass carbon is characterized by XRD (Figure S4a), which shows two peaks, one centered around 24° with a broad and strong peak and the other around 43° with a narrow and weak peak, corresponding to the (002) and (100) crystal planes of the graphitic phase carbon of a disordered structure. The Raman test shows two distinct characteristic peaks between MnO_2/BC and BC at 1309 cm^{-1} and 1570 cm^{-1}, which are the characteristic D and G bands, respectively (Figure S4b). In the low-frequency range, the characteristic peak centered at 638 cm^{-1} is the Mn-O bond vibration, confirming the presence of MnO_2 in the composite. In Raman spectra, the I_D/I_G intensity ratio reflects the degree of the amorphous nature of the synthetic material. The higher g-band (IG) intensity in BC indicates its higher graphitized carbon, ensuring the low resistance of BC during charge and discharge [49].

The synthesized porous biomass carbon was tested electrochemically in 1 M Na_2SO_4 at a potential of −1-0 V., and the GCD curve of BC shows a typical double-layer

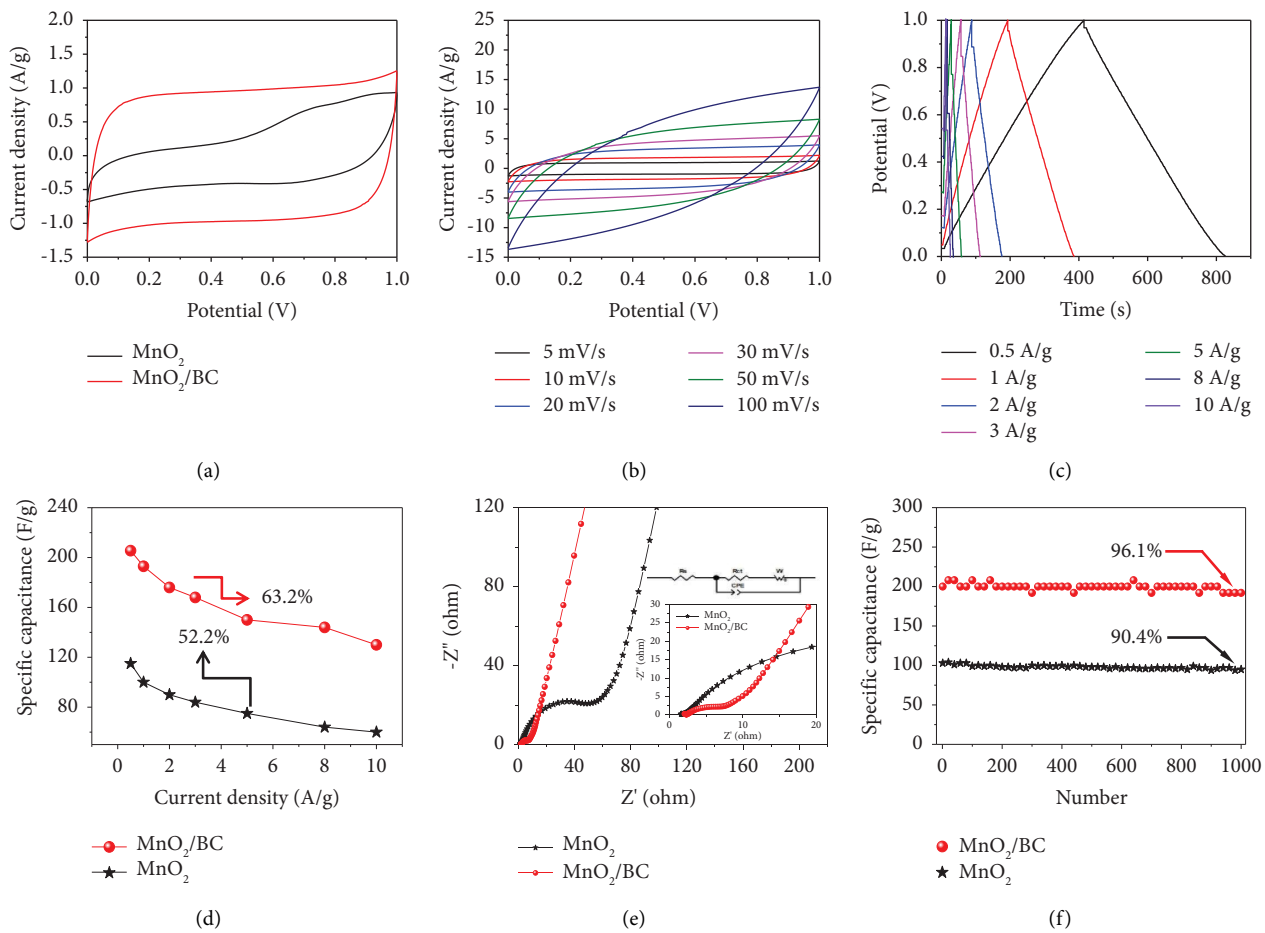

Figure 2: Comparison of CV curves of pure MnO_2 and composite materials (a); CV (b) of the composite at 5–100 mV·s^{-1}; GCD curve of MnO_2/BC electrode material (c); magnification plot of two electrode materials (d); the EIS diagram of the prepared electrode material, and the inset is the magnified diagram of part of the high frequency region and the low-frequency region and the simulated equivalent circuit diagram (e); long cycle curve of two materials (f).

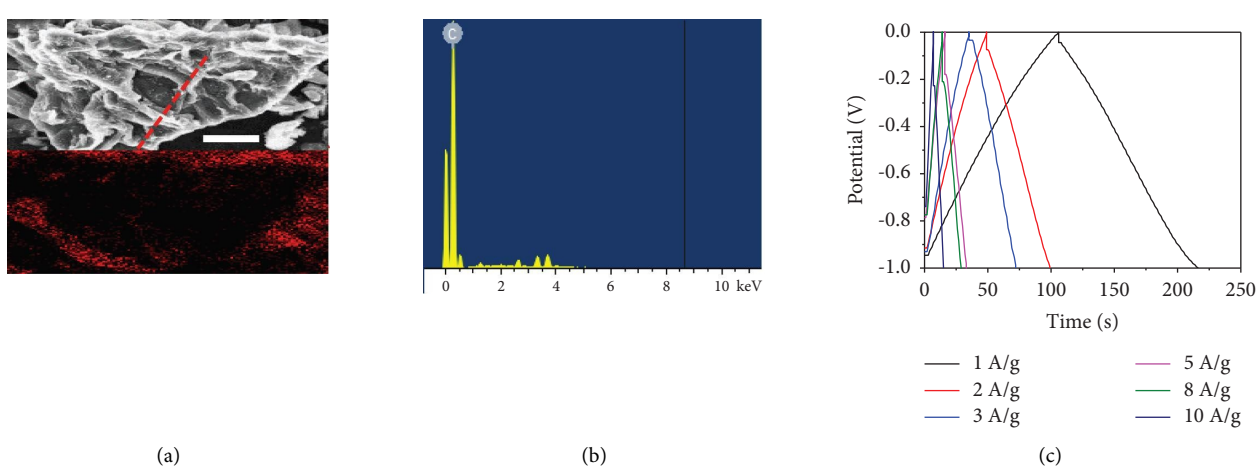

Figure 3: Continued.

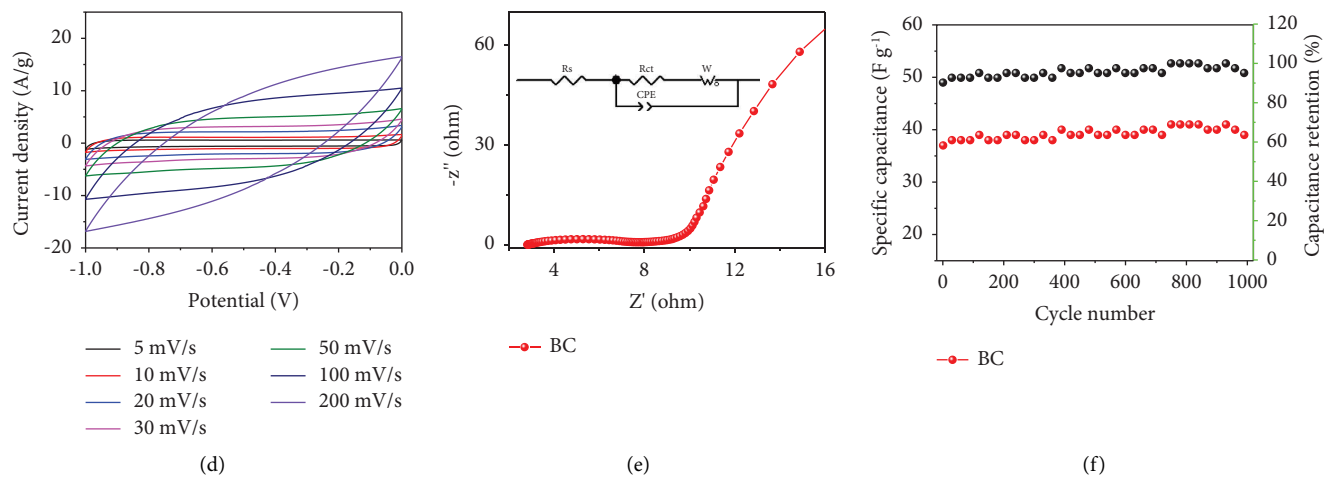

Figure 3: Scanning (a) and elemental analysis (b) of synthetic biomass carbon BC, the scale bar is 20 μm; the constant current charge-discharge curve of BC material (c); CV curve (d); impedance cardiography, and the inset is the simulated equivalent circuit diagram (e); cyclic performance (f).

charging and discharging behavior. The corresponding specific capacitance of the BC electrode material at the current density of 1, 2, 3, 5, 8, and 10 A·g^{-1} is 110, 100, 93, 85, 80, and 70 F·g^{-1}, respectively (Figure 3(c)). At large magnification, there is a significant voltage drop. The curve shape did not change as the sweep speed increased from 5 mV·s^{-1} to 200 mV·s^{-1} (Figure 3(d)). Meanwhile, the impedance spectrum in the frequency range of 10^{-2} Hz to 10^{5} Hz shows that the diffusion resistance (W) and charge transfer resistance (Rct) of the BC electrode material are small. The equivalent circuit diagram is further obtained based on the careful simulation of the resistance curves (the inset of Figure 3(e)), in which the Rs, Rct, and W values of the BC electrode were 1.55 Ω, 13.53 Ω, and 37.46 Ω, respectively, indicating the rapid charge transfer and ion diffusion of the biomass carbon material (Figure 3(e)). In addition, after continuous charging and discharging at 3 A/g, we found that the synthesized biomass carbon material could still maintain 100% of the initial capacitance, indicating the excellent long-cycle stability of the synthesized biomass carbon material (Figure 3(f)).

In order to evaluate the effect of MnO_2/BC composite in practical application, asymmetric supercapacitors was assembled with MnO_2/BC composite as the positive electrode and biomass carbon (BC) synthesized from grapefruit skin as the corresponding negative electrode. In order to determine the voltage range of the whole cell, CV tests were performed for the positive and negative electrode materials, respectively (Figure 4(a)). When the scan speed was 20 mV·s^{-1}, the voltage range of BC and MnO_2/BC composite was −1-0 V and 0-1 V, respectively. Therefore, the voltage window range of the assembled whole cell was determined to be 0–2 V. To examine the enhanced electrochemical performance after the composite biomass carbon material, CV tests performed on the whole cell composed of two electrode materials at 20 mV·s^{-1}. Both electrode materials exhibit a rectangular shape at 20 mV·s^{-1}. However, the full cell composed of MnO_2/BC combined with biomass carbon exhibits a larger capacitance relative to pure MnO_2 (Figure 4(b)). The CV test of the two electrode materials at 45–100 mV·s^{-1} (Figures S5a and S5b), which also presents intuitively that MnO_2/BC composite has a larger capacitance than pure manganese dioxide. To detect its actual capacitance, the GCD test was carried out on the whole battery constructed by two different materials (Figure S5). When the asymmetric SCs constructed by composite materials were 0.2, 0.5, 1, 2, and 3 A·g^{-1}, the capacities displayed were 60, 53.75, 39, 30, and 27 F·g^{-1}, respectively. Even when the current density reaches 25 times the initial value, the specific capacitance of the whole cell can still reach 25 F·g^{-1}, indicating the great potential of this all-cell device in practical applications (Figure 4(c)).

To distinguish the electrical conductivity of the device that can be enhanced after compound BC in the electrochemical test process, the EIS test is conducted (Figure 4(d)). The asymmetric SCs constructed by the MnO_2/BC composite electrode material and BC show smaller semicircles and steeper straight lines, indicating its better ionic and electronic conductivity. To express the relationship between the energy density (E) and power density (P) of asymmetric SCs, the Ragone curve is used (Figure 4(e)). It shows that at any power density, asymmetric SCs assembled by positive and negative materials with active materials of composite BC show greater energy density. The maximum E value can reach 33.3 W·h·kg^{-1}, even when the P value is 5000 W·kg^{-1}, and the energy density can also reach 13.9 W·h·kg^{-1}. Such a high energy density is due to its high capacitance and 2.0 V large voltage window according to the following equation:

$$E = 0.5\ CV^2, \tag{2}$$

where E represents the energy density of the asymmetric supercapacitor device, C is used to represent the capacitance that can be stored by the device, and V represents the voltage window of the entire device in the drainage electrolyte. At the same time, the power density can be calculated based on the equation (2) as follows:

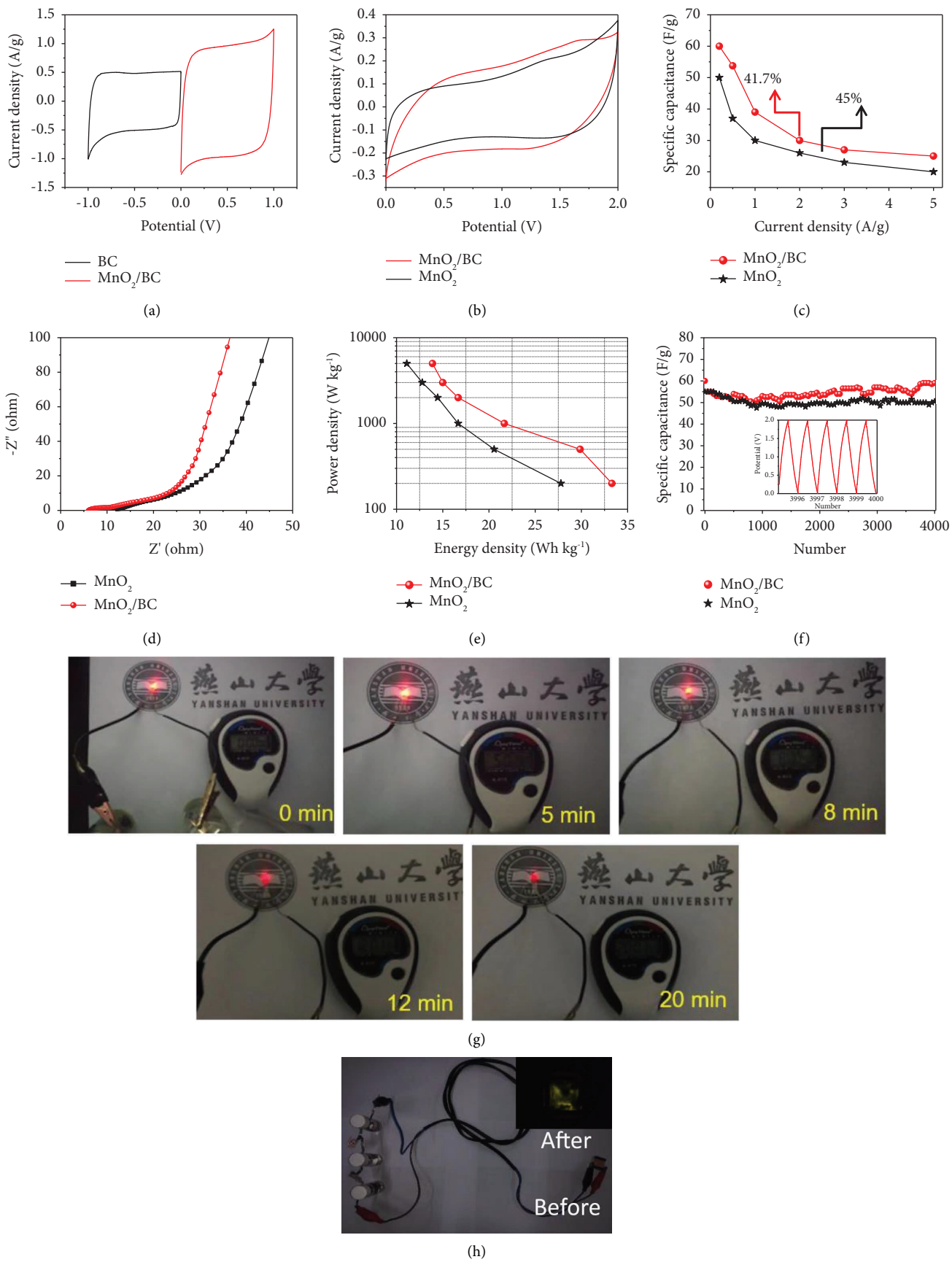

Figure 4: CV curves of BC and MnO_2/BC at 20 mV·s^{-1} (a); CV curves of two whole cells at 20 mV·s^{-1} (b); the magnification plot of the two full cells (c); the EIS plot of the asymmetric supercapacitor constructed (d); Ragone (E-P) curve (e); long-cycle curve (f); luminance photos of light-emitting diodes at different times (g); three 2.0 V asymmetric supercapacitors were connected in series and used to light up a yellow electrochemical light-emitting device with RUB as the light-emitting active layer (h).

$$P = \frac{E}{t}. \quad (3)$$

Here, P stands for power density and T stands for time.

Under 0.5 A·G^{-1}, the coulomb efficiency remains 100% even after 4000 cycles (the inset of Figure 4(f)). Besides, it can be observed that after 4000 times of continuous charging and discharging, the whole cell constructed by composite materials and biomass carbon shows better cycle stability, which can reach 105% of the initial capacitance, indicating that the electrode material obtained by composite BC shows better electrochemical performance, as compared to the recently reported supercapacitor device [58–69] (Figure 4(f)).

In order to understand the performance of the full battery in practical applications, two 2.0 V asymmetric supercapacitors were connected in series and examined. The device after series still shows excellent electrochemical performance under the voltage window of 0–4 V, and the CV tests at different sweep speeds show excellent magnification performance (Figure S7a). The constant current charge and discharge test shows that the discharge time of two devices in series is twice that of one device, indicating a small capacitance loss after series (Figure S7b). Two full-cell self-assembled devices with a 4.0 V large voltage window were used to test their performance in practical applications (Figure 4(g)). It charged continuously three times at 1 A·g^{-1} and then connected to a red LED. The light-emitting process of the diode from bright to dark lasted for 20 minutes. Besides, we used two series of asymmetric supercapacitors to light up the pure bromoperovskite light-emitting device, which shows that the series of 4.0 V full battery could make the pure bromoperovskite from colorless to black (Figure S8). Since the asymmetric supercapacitor can combine the voltage window of the positive and negative electrodes, there are a large voltage window of 2.0 V and its own large specific capacitance. The constructed asymmetric supercapacitor shows a high energy density of 33.3 Wh·kg^{-1} (power density of 200 W·kg^{-1}), which is also the reason that it can light a small bulb for 20 minutes. Three 2.0 V asymmetric supercapacitors were connected in series and used to light up a yellow electrochemical light-emitting device with Rubrene (RUB) as the light-emitting active layer, and excellent light-emitting effects were found. The excellent performance in the field of supercapacitor energy storage and perovskite discoloration gives us a reason to believe that the composite of carbon materials with high conductivity can still be an excellent solution to the problem of poor conductivity of Mn oxides.

4. Conclusions

In conclusion, we composited the porous, high-specific surface area biomass carbon material (BC) prepared by the carbonization of grapefruit peel with MnO_2 and successfully prepared the anode material of high conductivity asymmetric SCs. The sea urchin-like MnO_2/BC composites were achieved by the direct growth of nanorods MnO_2 on the BC surface by using a simple hydrothermal method. Based on the unique sea urchin-like structure of the materials themselves, the MnO_2/BC electrode material has a large specific surface area and high conductivity carbon material. The introduction of biomass carbon with strong electrical conductivity can greatly increase the electrical conductivity of the whole system. In addition, the structure combined with two-dimensional nanosheets provides more active surface, which is conducive to the enhancement of electrochemical performance. After the composite of BC, the MnO_2/BC electrode material not only obtained a higher specific capacitance value compared with the pure MnO_2, but also the resistance of the material became smaller. In addition, the asymmetric supercapacitor constructed from MnO_2/BC positive and BC negative materials showed good long cycling ability after 4000 continuous charging and discharging cycles. The specific capacitance of the MnO_2/BC composites' electrode can reach 205.5 F·g^{-1} when the charge-discharge current density is 0.5 A·g^{-1}. Considering the simple synthesis of the biomass carbon material and the excellent electrochemical performance of the obtained composite electrode materials, the method of enhancing the electrochemical performance by composite carbon materials is still attractive in the future.

Data Availability

The datasets used in this paper are available from the corresponding author upon request.

Conflicts of Interest

The authors declare that they have no conflicts of interest.

Authors' Contributions

Xiaoyu Zhao and Ning Wang contributed equally to this work.

Acknowledgments

This work was supported by the Natural Science Foundation of Heilongjiang Province of China (No. LH2022B025), Fundamental Research Funds for the Provincial Universities of Heilongjiang Province (No. KYYWF10236190104), Natural Science Foundation of Hebei Province (No. B2020203013), and Youth Foundation of Hebei Educational Committee (No. QN2020137).

Supplementary Materials

This material is available free of charge. The EDS mapping, N_2 sorption-desorption isotherms, the values of b in Logi = blogv + Log, XRD pattern, Raman spectra, full cell, the charge and discharge curve, cyclic voltammetry curves, charge-discharge diagram, the electrochromic device, specific surface area versus pore volume, equivalent circuit diagrams, and the summary of cycling stability. (*Supplementary Materials*)

References

[1] X. Huang, K. Yin, S. Zhang et al., "Interfacial chemical bond-modulated Z-scheme $Cs_2AgBiBr_6/WO_3$ enables stable and highly efficient photocatalysis," *Applied Surface Science*, vol. 637, Article ID 157877, 2023.

[2] M. Xu, J. Gu, Z. Fang, Y. Li, X. Wang, and X. Zhao, "Colorless to black switching with high contrast ratio via the electrochemical process of a hybrid organic–inorganic perovskite," *Carbon Energy*, vol. 2023, p. e358.

[3] L. Li, J. Nam, M. Kim et al., "Sulfur-carbon electrode with PEO-LiFSI-PVDF composite coating for high-rate and long-life lithium-sulfur batteries," *Advanced Energy Materials*, vol. 13, no. 36, Article ID 2302139, 2023.

[4] G. Zeng, Y. Wang, X. Lou, H. Chen, S. Jiang, and W. Zhou, "Vanadium oxide/carbonized chestnut needle composites as cathode materials for advanced aqueous zinc-ion batteries," *Journal of Energy Storage*, vol. 77, Article ID 109859, 2024.

[5] W. Deng, Y. Xu, X. Zhang et al., "$(NH4)2Co_2V_{10}O_{28}\cdot16H_2O/(NH_4)_2V_{10}O_{25}\cdot8H_2O$ heterostructure as cathode for high-performance aqueous Zn-ion batteries," *Journal of Alloys and Compounds*, vol. 903, Article ID 163824, 2022.

[6] W. Deng, W. Liu, H. Zhu, L. Chen, H. Liao, and H. Chen, "Click-chemistry and ionic cross-linking induced double cross-linking ionogel electrolyte for flexible lithium-ion batteries," *Journal of Energy Storage*, vol. 72, Article ID 108509, 2023.

[7] W. Deng, Y. Li, D. Xu, W. Zhou, K. Xiang, and H. Chen, "Three-dimensional hierarchically porous nitrogen-doped carbon from water hyacinth as selenium host for high-performance lithium–selenium batteries," *Rare Metals*, vol. 41, no. 10, pp. 3432–3445, 2022.

[8] X. Wen, J. Luo, K. Xiang, W. Zhou, C. Zhang, and H. Chen, "High-performance monoclinic WO_3 nanospheres with the novel NH_4^+ diffusion behaviors for aqueous ammonium-ion batteries," *Chemical Engineering Journal*, vol. 458, Article ID 141381, 2023.

[9] W. Zhou, G. Zeng, H. Jin et al., "Bio-template synthesis of V_2O_3@carbonized dictyophora composites for advanced aqueous zinc-ion batteries," *Molecules*, vol. 28, no. 5, p. 2147, 2023.

[10] Z. Guo, X. Han, C. Zhang et al., "Activation of biomass-derived porous carbon for supercapacitors: a review," *Chinese Chemical Letters*, Article ID 109007, 2023.

[11] T. Guo, K. Xiang, X. Wen, W. Zhou, and H. Chen, "Facile construction on flower-like CuS microspheres and their applications for the high-performance aqueous ammonium-ion batteries," *Materials Research Bulletin*, vol. 170, Article ID 112595, 2024.

[12] X. Ma, S. Liu, H. Luo et al., "MOF@wood derived ultrathin carbon composite film for electromagnetic interference shielding with effective absorption and electrothermal management," *Advanced Functional Materials*, vol. 34, no. 4, Article ID 2310126, 2023.

[13] X. Wei, Q. Wu, L. Chen et al., "Remotely controlled light/electric/magnetic multiresponsive hydrogel for fast actuations," *American Chemical Society Applied Materials and Interfaces*, vol. 15, no. 7, pp. 10030–10043, 2023.

[14] C. V. Reddy, R. R. Kakarla, B. Cheolho, J. Shim, and T. M. Aminabhavi, "Heterostructured 2D/2D $ZnIn_2S_4$/g-C_3N_4 nanohybrids for photocatalyticdegradation of antibiotic sulfamethoxazole andphotoelectrochemical properties," *Environmental Research*, vol. 225, Article ID 115585, 2023.

[15] M. R. Tamtam, R. Koutavarapu, and J. Shim, "$InVO_4$ nanosheets decorated with $ZnWO_4$ nanorods: a novel composite andits enhanced photocatalytic performance under solar light," *Environmental Research*, vol. 227, Article ID 115735, 2023.

[16] B. Akkinepally, N. R. Nadar, I. Neelakanta Reddy, H. Jeevan Rao, K. S. Nisar, and J. Shim, "Unlocking enhanced electrochemical performance of SnO_2-Bi_2WO_6 nanoflowers for advanced supercapacitor device," *Journal of Alloys and Compounds*, vol. 970, Article ID 172677, 2024.

[17] K. Poonam, K. Sharma, A. Arora, and S. Tripathi, "Review of supercapacitors: materials and devices," *Journal of Energy Storage*, vol. 21, pp. 801–825, 2019.

[18] J. Gu, X. Fan, X. Liu et al., "Mesoporous manganese oxide with large specific surface area for high-performance asymmetric supercapacitor with enhanced cycling stability," *Chemical Engineering Journal*, vol. 324, no. 15, pp. 35–43, 2017.

[19] Z. Wang, J. Gu, S. Li et al., "One-step polyoxometalates-assisted synthesis of manganese dioxide for asymmetric supercapacitors with enhanced cycling lifespan," *American Chemical Society Sustainable Chemistry and Engineering*, vol. 7, no. 1, pp. 258–264, 2019.

[20] F. Zhang, R. Zhao, Y. Wang et al., "Superwettable surface-dependent efficiently electrocatalytic water splitting based on their excellent liquid adsorption and gas desorption," *Chemical Engineering Journal*, vol. 452, Article ID 139513, 2023.

[21] B. Yin, J. Liang, J. Hao et al., "Nonconfinement growth of edge-curved molecular crystals for self-focused microlasers," *Science Advances*, vol. 8, no. 42, Article ID eabn8106, 2022.

[22] M. Fu, Z. Zhu, Z. Zhang et al., "Microwave assisted growth of MnO_2 on biomass carbon for advanced supercapacitor electrode materials," *Journal of Materials Science*, vol. 56, no. 11, pp. 6987–6996, 2021.

[23] H. Wang, G. Yan, X. Cao et al., "Hierarchical $Cu(OH)_2$@MnO_2core-shell nanorods array in situ generated on three-dimensional copper foam for high performance supercapacitors," *Journal of Colloid and Interface Science*, vol. 563, pp. 394–404, 2020.

[24] Z. Deng, X. Huang, X. Zhao, H. Cheng, and H. Wang, "Facile synthesis of hierarchically structured manganese oxides as anode for lithium-ion batteries," *Journal of Central South University*, vol. 26, no. 6, pp. 1481–1492, 2019.

[25] H. Quan, W. Zeng, W. Chen, Y. Wang, W. Tao, and D. Chen, "Carbon quantum dot-induced robust ε-MnO_2 electrode by synergistic engineering of oxygen vacancy and low crystallinity for high-performance flexible asymmetric supercapacitor," *Journal of Alloys and Compounds*, vol. 938, Article ID 168524, 2023.

[26] W. Zeng, H. Quan, J. Meng, W. Wei, M. Liu, and D. Chen, "Nitrogen plasma activation of cactus-like MnO_2 grown on carbon cloth for high-mass loading asymmetric supercapacitors," *Applied Surface Science*, vol. 572, Article ID 151323, 2022.

[27] Y. Chen, C. Jing, X. Fu et al., "In-situ fabricating MnO_2 and its derived FeOOH nanostructures on mesoporous carbon towards high-performance asymmetric supercapacitor," *Applied Surface Science*, vol. 503, Article ID 144123, 2020.

[28] M. Fu, W. Chen, X. Zhu, B. Yang, and Q. Liu, "Crab shell derived multi-hierarchical carbon materials as a typical recycling of waste for high performance supercapacitors," *Carbon*, vol. 141, pp. 748–757, 2019.

[29] C. Miao, C. Zhou, H. Wang et al., "Hollow Co–Mo–Se nanosheet arrays derived from metal-organic framework for

high-performance supercapacitors," *Journal of Power Sources*, vol. 490, Article ID 229532, 2021.

[30] J. Ren, M. Shen, Z. Li et al., "Towards high-performance all-solid-state asymmetric supercapacitors: a hierarchical doughnut-like Ni_3S_2@PPy core–shell heterostructure on nickel foam electrode and density functional theory calculations," *Journal of Power Sources*, vol. 501, Article ID 230003, 2021.

[31] P. Wang, X. Ding, R. Zhe et al., "Synchronous defect and interface engineering of $NiMoO_4$ nanowire arrays for high-performance supercapacitors," *Nanomaterials*, vol. 12, no. 7, p. 1094, 2022.

[32] L. Zheng, Y. Zhao, P. Xu et al., "Copper doped CoSx@Co(OH)$_2$ hierarchical mesoporous nanosheet arrays as binder-free electrodes for superior supercapacitors," *Journal of Alloys and Compounds*, vol. 911, Article ID 165115, 2022.

[33] M. Fu, Z. Zhu, Z. Zhang, Q. Zhuang, W. Chen, and Q. Liu, "Microwave deposition synthesis of $Ni(OH)_2$/sorghum stalkbiomass carbon electrode materials for supercapacitors," *Journal of Alloys and Compounds*, vol. 846, Article ID 156376, 2020.

[34] C. Qin, S. Wang, Z. Wang et al., "Hierarchical porous carbon derived from gardenia jasminoides ellis flowers for high performance supercapacitor," *Journal of Energy Storage*, vol. 33, Article ID 102061, 2021.

[35] Y. Zhou, X. Zhou, C. Ge, W. Zhou, Y. Zhu, and B. Xu, "Branched carbon nanotube/carbon nanofiber composite for supercapacitor electrodes," *Materials Letters*, vol. 246, pp. 174–177, 2019.

[36] M. El-Kady, Y. Shao, and R. Kaner, "Graphene for batteries, supercapacitors and beyond," *Nature Review Materials*, vol. 1, no. 7, Article ID 16033, 2016.

[37] F. Cheng, X. Yang, S. Zhang, and W. Lu, "Boosting the supercapacitor performances of activated carbon with carbon nanomaterials," *Journal of Power Sources*, vol. 450, Article ID 227678, 2020.

[38] J. Deng, J. Li, S. Song, Y. Zhou, and L. Li, "Electrolyte-dependent supercapacitor performance on nitrogen-doped porous bio-carbon from gelatin," *Nanomaterials*, vol. 10, no. 2, p. 353, 2020.

[39] L. Zheng, M. Chen, S. Liang, and Q. F. Lü, "Oxygen-rich hierarchical porous carbon derived from biomass waste-kapok flower for supercapacitor electrode," *Diamond and Related Materials*, vol. 113, Article ID 108267, 2021.

[40] R. Senthil, V. Yang, J. Pan, and Y. Sun, "A green and economical approach to derive biomass porous carbon from freely available feather finger grass flower for advanced symmetric supercapacitors," *Journal of Energy Storage*, vol. 35, Article ID 102287, 2021.

[41] M. Vinayagam, R. Suresh Babu, A. Sivasamy, and A. L. Ferreira de Barros, "Biomass-derived porous activated carbon from syzygium cumini fruit shells and chrysopogon zizanioides roots for high-energy density symmetric supercapacitors," *Biomass and Bioenergy*, vol. 143, Article ID 105838, 2020.

[42] Z. Li, D. Guo, Y. Liu, H. Wang, and L. Wang, "Recent advances and challenges in biomass-derived porous carbon nanomaterials for supercapacitors," *Chemical Engineering Journal*, vol. 397, Article ID 125418, 2020.

[43] Y. Xu, H. Lei, S. Qi et al., "Three-dimensional zanthoxylum leaves-derived nitrogen-doped porous carbon frameworks for aqueous supercapacitor with high specific energy," *Journal of Energy Storage*, vol. 32, Article ID 101970, 2020.

[44] X. Yuan, Y. Zhang, Y. Yan et al., "Tunable synthesis of biomass-based hierarchical porous carbon scaffold@MnO_2 nanohybrids for asymmetric supercapacitor," *Chemical Engineering Journal*, vol. 393, Article ID 121214, 2020.

[45] G. J. Yang and S. J. Park, "MnO_2 and biomass-derived 3D porous carbon composites electrodes for high performance supercapacitor applications, J. Alloy," *Journal of Alloys and Compounds*, vol. 741, pp. 360–367, 2018.

[46] G. Yang and S. J. Park, "Nanoflower-like $NiCo_2O_4$ grown on biomass carbon coated nickel foam for asymmetric supercapacitor," *Journal of Alloys and Compounds*, vol. 835, Article ID 155270, 2020.

[47] G. Yang and S. J. Park, "Facile hydrothermal synthesis of $NiCo_2O_4$-decorated filter carbon as electrodes for high-performance asymmetric supercapacitors," *Electrochimica Acta*, vol. 285, pp. 405–414, 2018.

[48] Z. Huang, Y. Song, D. Feng, Z. Sun, X. Sun, and X. Liu, "High mass loading MnO_2 with hierarchical nanostructures for supercapacitors," *Journal of Central South University Nano*, vol. 12, no. 4, pp. 3557–3567, 2018.

[49] Z. Ni, X. Liang, L. Zhao, H. Zhao, B. Ge, and W. Li, "Tin doping manganese dioxide cathode materials with the improved stability for aqueous zinc-ion batteries," *Materials Chemistry and Physics*, vol. 287, Article ID 126238, 2022.

[50] K. Xiao, L. X. Ding, H. Chen, S. Wang, X. Lu, and H. Wang, "Nitrogen-doped porous carbon derived from residuary shaddock peel: a promising and sustainable anode for high Energy density asymmetric supercapacitors," *Journal of Materials Chemistry A*, vol. 4, no. 2, pp. 372–378, 2016.

[51] J. Du, Y. Zhang, H. Lv, and A. Chen, "Silicate-assisted activation of biomass towards N-doped porous carbon sheets for supercapacitors," *Journal of Alloys and Compounds*, vol. 853, Article ID 157091, 2021.

[52] R. Hossain, R. Nekouei, I. Mansuri, and V. Sahajwalla, "In-situ O/N-heteroatom enriched activated carbon by sustainable thermal transformation of waste coffee grounds for supercapacitor material," *Journal of Energy Storage*, vol. 33, Article ID 102113, 2021.

[53] H. Liu, Z. Yao, Y. Liu et al., "In situ synthesis of nitrogen site activated cobalt sulfide@N, S dual-doped carbon composite for a high-performance asymmetric supercapacitor," *Journal of Colloid and Interface Science*, vol. 585, pp. 30–42, 2021.

[54] J. Yan, J. Shen, L. Li et al., "Template-like N, S and O tri-doping activated carbon derived from helianthus pallet as high-performance material for supercapacitors," *Diamond and Related Materials*, vol. 102, Article ID 107693, 2020.

[55] W. Chen, H. Quan, and D. Chen, "Carbon quantum dots boosted structure stability of nickel cobalt layered double hydroxides nanosheets electrodeposited on carbon cloth for energy storage," *Surfaces and Interfaces*, vol. 36, Article ID 102498, 2023.

[56] W. Luo, W. Chen, H. Quan et al., "Strongly coupled carbon quantum dots/NiCo-LDHs nanosheets on carbon cloth as electrode for high performance flexible supercapacitors," *Applied Surface Science*, vol. 591, Article ID 153161, 2022.

[57] F. Raj, G. Boopathi, N. Jaya, D. Kalpana, A. Pandurangan, and S. N, "N, S codoped activated mesoporous carbon derived from the Datura metel seed pod as active electrodes for supercapacitors," *Diamond and Related Materials*, vol. 102, Article ID 107687, 2020.

[58] X. Ma, J. Pan, H. Guo et al., "Ultrathin wood-derived conductive carbon composite film for electromagnetic shielding and electric heating management," *Advanced Functional Materials*, vol. 33, no. 16, p. 2213, 2023.

[59] G. Duan, J. Xiao, L. Chen et al., "Zinc gluconate derived porous carbon electrode assisted high rate and long cycle performance supercapacitor," *Journal of Energy Storage*, vol. 67, Article ID 107559, 2023.

[60] Z. Tian, Z. Weng, J. Xiao, F. Wang, C. Zhang, and S. Jiang, "Hierarchically porous carbon nanosheets from one-step carbonization of zinc gluconate for high-performance supercapacitors," *International Journal of Molecular Sciences*, vol. 24, no. 18, Article ID 14156, 2023.

[61] H. Li, L. Cao, H. Zhang et al., "Intertwined carbon networks derived from Polyimide/Cellulose composite as porous electrode for symmetrical supercapacitor," *Journal of Colloid and Interface Science*, vol. 609, pp. 179–187, 2022.

[62] F. Wang, L. Chen, H. Li et al., "N-doped honeycomb-like porous carbon towards high-performance supercapacitor," *Chinese Chemical Letters*, vol. 31, no. 7, pp. 1986–1990, 2020.

[63] L. Cao, H. Li, X. Liu et al., "Nitrogen, sulfur co-doped hierarchical carbon encapsulated in graphenewith "sphere-in-layer" interconnection for high-performance supercapacitor," *Journal of Colloid and Interface Science*, vol. 599, pp. 443–452, 2021.

[64] J. Yang, H. Li, S. He et al., "Facile electrodeposition of $NiCo_2O_4$ nanosheets on porous carbonized wood for wood-derived asymmetric supercapacitors," *Polymers*, vol. 14, no. 13, p. 2521, 2022.

[65] W. Guo, X. Guo, L. Yang et al., "Synthetic melanin facilitates MnO supercapacitors with high specific capacitance and wide operation potential window," *Polymer*, vol. 235, Article ID 124276, 2021.

[66] G. Duan, L. Zhao, L. Chen et al., "$ZnCl_2$ regulated flax-based porous carbon fibers for supercapacitors with good cycling stability," *New Journal of Chemistry*, vol. 45, no. 48, pp. 22602–22609, 2021.

[67] A. Manohar, V. Vijayakanth, S. P. Vattikuti, G. R. Reddy, and K. H. Kim, "A brief review on Zn-based materials and nanocomposites for supercapacitor applications," *Journal of Energy Storage*, vol. 68, Article ID 107674, 2023.

[68] S. V. P. Vattikuti, C. T. Hoang Ngoc, H. Nguyen, N. H. Nguyen Thi, J. Shim, and N. N. Dang, "Carbon nitride coupled Co_3O_4: a pyrolysis-based approach for high-performance hybrid energy storage," *Journal of Physical Chemistry Letters*, vol. 14, no. 42, pp. 9412–9423, 2023.

[69] S. P. Vattikuti, J. Zeng, J. Shim, D. S. Lee, and K. C. Devarayapalli, "Facile synthesis of ultrathin $Bi(OH)SO_4{\cdot}H_2O$ nanosheets and battery-like electrode for symmetric supercapacitors," *Journal of Alloys and Compounds*, vol. 936, Article ID 168186, 2023.